metals

MDPI

Article

Predicting the Ti-Al Binary Phase Diagram with an Artificial Neural Network Potential

Micah Nichols [1,2], Mashroor S. Nitol [3], Saryu J. Fensin [3], Christopher D. Barrett [1,2] and Doyl E. Dickel [1,2,*]

[1] Michael W. Hall School of Mechanical Engineering, Mississippi State University, Starkville, MS 39762, USA; mwn45@msstate.edu (M.N.); barrett@me.msstate.edu (C.D.B.)
[2] Center for Advanced Vehicular Systems, Mississippi State University, Starkville, MS 39762, USA
[3] Los Alamos National Laboratory, Los Alamos, NM 87545, USA
* Correspondence: doyl@me.msstate.edu

Abstract

The microstructure of the Ti-Al binary system is an area of great interest, as it affects material properties and plasticity. Phase transformations induce microstructural changes; therefore, accurately modeling the phase transformations of the Ti-Al system is necessary to describe plasticity. Interatomic potentials can be a powerful tool to model how materials behave; however, existing potentials lack accuracy in certain aspects. While classical potentials like the Modified Embedded Atom Method (MEAM) perform adequately for modeling a dilute Al solute within Ti's α phase, they struggle with accurately predicting plasticity. In particular, they struggle with stacking fault energies in intermetallics and to some extent elastic properties. This hinders their effectiveness in investigating the plastic behavior of formed intermetallics in Ti-Al alloys. Classical potentials also fail to predict the α-to-β phase boundary. Existing machine learning (ML) potentials reproduce the properties of formed intermetallics with density functional theory (DFT) but do not accurately capture the α-to-β or α-to-$D0_{19}$ phase boundaries. This work uses a rapid artificial neural network (RANN) framework to produce a neural network potential for the Ti-Al binary system. This potential is capable of reproducing the Ti-Al binary phase diagram up to 30% Al concentration. The present interatomic potential ensures stability and allows results near the accuracy of DFT. Using Monte Carlo simulations, the RANN potential accurately predicts the α-to-β and α-to-$D0_{19}$ phase transitions. The current potential also exhibits accurate elastic constants and stacking fault energies for the $L1_0$ and $D0_{19}$ phases.

Keywords: titanium; aluminum; phase transition; molecular dynamics; machine learning; intermetallics

Check for updates

Academic Editor: Wenchao Yang

Received: 16 December 2025
Revised: 15 January 2026
Accepted: 21 January 2026
Published: 24 January 2026

Copyright: © 2026 by the authors. Licensee MDPI, Basel, Switzerland. This article is an open access article distributed under the terms and conditions of the Creative Commons Attribution (CC BY) license.

1. Introduction

Ti-Al alloys are indispensable due to their high melting points, exceptional specific strength and stiffness, and excellent resistance to oxidation and corrosion [1]. These properties make them suitable for load-carrying applications in the aerospace, automotive, and energy industries [2,3]. While Ni-based superalloys have traditionally dominated these fields, Ti-Al alloys exhibit comparable performances at temperatures ranging between 600 and 800 °C [4]. The ability of Ti-Al alloys, particularly the two-phase intermetallics like $L1_0$ γ-TiAl and $D0_{19}$ α_2-Ti_3Al, to operate efficiently at elevated temperatures while maintaining resistance to oxidation and creep underscores their technological importance [5,6]. The microstructure within Ti-Al alloys changes significantly with composition. At low Al concentrations, Ti has a low-temperature α (HCP) phase and a high-temperature β (BCC)

phase. At an Al concentration around 12%, the ordered hexagonal $D0_{19}$ (α_2) phase forms. These phases and their corresponding Al concentrations affect material properties such as ductility, fracture toughness, and creep resistance. Guo et al. [7] show that creep resistance in the α phase increases with increasing Al concentration due to the decrease in the stacking fault energy along the basal plane. Lamellar γ-TiAl, with a combination of γ and α_2 phases, exhibits superior high-temperature performance but suffers from poor room-temperature ductility due to its complex dislocation slip and twinning systems [8]. Introducing a small amount (10–20%) of the β phase within a matrix of the α phase can combine the creep resistance of the α phase with the increased strength of the β phase [9]. Studying the phases within Ti-Al alloys is crucial for understanding and enhancing their mechanical behavior under operational conditions. Phase transformations dictate the material's structural integrity and performance, particularly under thermal cycling, which is common in aerospace applications [10,11]. Understanding these transformations helps in optimizing alloy compositions and heat treatment processes to achieve desired mechanical properties.

Molecular dynamics (MD) simulations play a pivotal role in the modeling of Ti-Al alloys by utilizing atomic-scale interactions to reproduce phenomena that can be challenging to observe experimentally. These simulations provide insights into the mechanisms of plastic deformation, phase transitions, and the impact of alloying elements on the material's properties. Furthermore, MD can predict the behavior of materials under various loading and environmental conditions, thus aiding in the design of more resilient materials. Both experimental and computational methodologies have been used in the extensive study of Ti-Al alloys to interpret the complex interplay of alloy composition, microstructure, and mechanical properties [12–14]. Historically, experimental approaches, such as in situ transmission electron microscopy (TEM) experiments, have provided significant insights into basic deformation mechanisms, interface strengthening behaviors, and crack nucleation and propagation in these alloys. These studies have elucidated the role of microstructural features like grain and interphase boundaries in governing plasticity and fracture behaviors [15,16].

Computational research efforts have primarily focused on the use of density functional theory (DFT) [14,17–19] and empirical or semi-empirical interatomic potentials such as the Embedded Atom Method (EAM) [20–22] and the Modified Embedded Atom Method (MEAM) [23–25] to describe the microstructural features in Ti-Al alloys. DFT calculations have shed light on the non-planar character of dislocation cores and their associated Peierls stresses, offering deep insights at the atomic scale. One major drawback of using these quantum mechanics-based methods is the computational demand required when simulating complex dislocations or large systems [26–28].

Empirical potentials, while useful in overcoming the size and time limitations of DFT, often fall short in accuracy. For instance, EAM and MEAM potentials have been tailored to capture the directional bonding essential for modeling Ti-Al alloys but have shown discrepancies in modeling the full spectrum of plasticity and fracture phenomena across different stable phases [29]. This has led to a partial understanding that lacks the ability to comprehensively predict material behavior under varied operational conditions, particularly at high temperatures.

To address these challenges, a paradigm shift has emerged in the field of materials science, wherein machine learning (ML) techniques are leveraged to develop interatomic potentials [30–37]. ML potentials represent a departure from conventional methods, minimizing reliance on physical or chemical intuition by interpolating mathematical functions using reference data obtained from DFT computations. This data-driven approach has revolutionized computational materials science, accelerating the discovery of new materials by accurately capturing the underlying physics of interatomic bonding. Some of the more

popular ML potentials include the spectral neighbor analysis method (SNAP), Gaussian approximation potentials (GAPs), spline-based neural network potentials (s-NNPs), and moment tensor potentials (MTPs) [31,38–40]. For the Ti-Al system, the most prominent ML potential employs the MTP [41] formalism and exhibits superior accuracy when compared to previous ML potentials [42]. While the MTP demonstrates excellent accuracy within the intermetallic phases, it struggles to accurately represent the α-β phase transformation and fails to accurately predict the effects of Al solutes on the plasticity of both the α and β phases. It has been shown that the generalized stacking fault energy (GSFE) of basal slip in Ti decreases with increasing Al concentration [7], while the MTP predicts the opposite trend. Both of these inconsistencies of the MTP will be demonstrated below.

Building on the foundation laid by previous research, the current study introduces significant advancements in the molecular dynamics simulation of Ti-Al alloys through the development and implementation of the rapid artificial neural network (RANN) framework [43–47]. This approach leverages machine learning to interpolate complex potential energy surfaces from a vast dataset derived from high-fidelity DFT calculations. Unlike previous interatomic potentials, RANN is capable of modeling both the dilute and intermetallic phases of Ti-Al alloys with a level of precision comparable to DFT calculations. RANN is also effective in seamlessly transitioning between different alloy phases without a loss in accuracy. This is particularly important for Ti-Al alloys, where phase evolution plays a critical role in determining material properties. To the best of the authors' knowledge, no existing interatomic potential comprehensively models both the dilute alloy and intermetallic phases of this crucial alloy at the atomistic scale. The current study bridges the gap between the modeling capabilities of dilute alloys and intermetallics of Ti-Al. Here, RANN is designed to be inherently flexible, enabling it to accurately predict phase behaviors, solute effects, and the thermomechanical properties of both dilute and intermetallic phases.

2. Methodology

2.1. First-Principles Calculations

A DFT database was created using version 6.3.2 of the Vienna Ab initio Simulation Package (VASP) [48]. The simulations utilized the generalized gradient approximation (GGA) with the Perdew–Burke–Ernzerhof (PBE) [49] exchange–correlation functional. A densely packed Monkhorst–Pack *k*-mesh was implemented to ensure accuracy and maintained a minimum distance between neighboring *k*-points of $2\pi \times 0.01\text{Å}^{-1}$ in reciprocal lattice units. The electronic wave functions were expanded using a kinetic energy cutoff of 520 eV, and a Gaussian smearing of 0.2 eV smoothed the integration over the Brillouin zone.

The database contains data with up to 15% equilibrium lattice distortion for BCC, FCC, HCP, *a*15, *β-Sn*, SC, and DC structures in pure forms of Ti and Al. It also contains up to 15% equilibrium lattice distortions for ordered intermetallic structures such as TiAl, $TiAl_2$, $TiAl_3$, and Ti_3Al. For all the previously mentioned structures, additional simulations displace the atoms by random vectors with a magnitude of up to 0.5 Å as well as random independent distortions of the simulation box lengths and angles up to $\pm$5% to simulate finite-temperature behavior. Dislocation cores, vacancies, free surfaces, and amorphous configurations for Ti, Al, and Ti-Al alloys were also included. It should be noted that no GSFE or phase transition data was used in the training of the Ti-Al RANN potential. A detailed table showing all data used for training can be found in the Supplemental Materials.

2.2. RANN

RANN uses a multilayer perceptron artificial neural network and begins with an input layer that captures a structural fingerprint, characterizing the local atomic environment for each atom based on the MEAM formalism [50–52]. A separate, independent neural network

is created for each atom type defined. The input layer contains structural fingerprints to describe the interaction between a specific atom and its neighbors of a specific type. In Ti-Al, for example, two types of structural fingerprints are employed—a pair interaction fingerprint and a three-body fingerprint. The pair interaction is described by

$$F_n = \sum_{j \neq i} \left(\frac{r_{ij}}{r_e} \right)^n e^{-\alpha_n \frac{r_{ij}}{r_e}} f_c \left(\frac{r_c - r_{ij}}{\Delta r} \right) S_{ij} \tag{1}$$

where r_e is the equilibrium nearest neighbor distance; r_c is a cutoff distance to determine the neighbors, j, of atom i; n is an integer; α_n is related to the bulk modulus, as used in MEAM [52]; f_c is a cutoff function; and S_{ij} is an angular screening term. A set of integers is chosen to represent n so that each integer within the set is used to create a unique neuron in the input layer. Note that depending on the particular fingerprint, the set of atoms, j, included in the summation can be restricted to include only atoms of a specified type or to include all atoms within r_c. The Ti neural network, for example, could include pair fingerprints that only consider neighboring Ti atoms, only neighboring Al atoms, or all neighboring atoms. In this way, the description of the local environment is made sensitive to the type of neighboring atoms. The three-body term is described by

$$\begin{aligned} G_{m,k} = \sum_{j,k} cos^m \theta_{jik} e^{-\beta_k \frac{r_{ij}+r_{ik}}{r_e}} f_c \left(\frac{r_c - r_{ij}}{\Delta r} \right) \\ \times f_c \left(\frac{r_c - r_{ik}}{\Delta r} \right) S_{ij} S_{ik} \end{aligned} \tag{2}$$

where m is an integer, θ_{jik} describes the angle between the vectors from atom i to atom j and atom i to atom k, and β_k determines the length scale. A set of non-negative integers is chosen to represent m, and a set of values is chosen to represent β_k so that each unique pairing of m and β_k becomes a neuron within the input layer. Each type of fingerprint uses angular screening to reduce the neighbor list, therefore improving computational efficiency. The input layer for each atom type is made of different structural fingerprints to describe each interaction. As with the pairwise fingerprints, the sum over j and k can independently consider either particular atoms types or all neighboring atoms. The cutoff function used in both types of fingerprints, $f_c(x)$, is the same at that used in MEAM [52] and smoothly transitions the weight of the interaction from 1 to 0 as the distance between atoms reaches the cutoff distance, r_c. It takes the form of

$$f_c(x) = \left\{ \begin{array}{ll} 1, & x > 1 \\ (1-(1-x)^4)^2, & 0 \leq x \leq 1 \\ 0, & x < 0 \end{array} \right\} \tag{3}$$

where Δr describes the width of the transition from 1 to 0. The angular screening term, S_{ij}, is employed to reduce the neighbor list, and therefore the computational time, without having to restrict the cutoff distance. This is accomplished by reducing or eliminating the interaction between atoms when another atom is located between the pair. The angular screening term between two atoms is the product of all the screening interactions for those two atoms:

$$S_{ij} = \prod_{k \neq i,j} S_{ikj} \tag{4}$$

where S_{ikj} is found by forming an ellipse between atoms i, k, and j and calculating the screening parameter, C_{ikj}. C_{ikj} can be found by

$$C_{ikj} = 1 + 2\frac{r_{ij}^2 r_{ik}^2 + r_{ij}^2 r_{jk}^2 - r_{ij}^4}{r_{ij}^4 - \left(r_{ik}^2 - r_{jk}^2\right)^2} \tag{5}$$

The screening value, S_{ikj} is then given by

$$S_{ikj} = f_c\left(\frac{C_{ikj} - C_{min}}{C_{max} - C_{min}}\right) \tag{6}$$

where C_{max} and C_{min} are tunable parameters that control the extent to which atoms get screened.

After the input layer made of structural fingerprints, RANN accepts an arbitrary number of hidden layers and one output layer that produces the energy for a particular atom. Each layer after the input layer is given by

$$A_{l_n}^n = g^n\left(Z_{l_n}^n\right) \tag{7}$$

where l_n represents the number of neurons in layer n and $g_n(x)$ represents a nonlinear activation function. $Z_{l_n}^n$ is found using the values of the previous layer along with the weight and bias matrices:

$$Z_{l_n}^n = \sum_{l_{n-1}} W_{l_n l_{n-1}}^n A_{l_{n-1}}^{n-1} + B_{l_n}^n \tag{8}$$

Here, A^{n-1} represents the values from the previous layer, W^n is the weight matrix, and B^n is the bias matrix. The output layer will always comprise a single node to represent the atomic energy. In this case, W^n will be a row vector and B^n will be a single number. The system energy is the sum of each individual atomic energy within the system. In total, 10% of the data from each sample set is reserved for validation purposes. This means that if the database contained sample set a and sample set b, 10% of sample set a and 10% of sample set b would be set aside for validation—not a random 10% of the whole database. The Levenberg–Marquardt (LM) algorithm [53,54], noted for its efficiency over traditional gradient descent methods in machine learning interatomic potentials (MLIPs) [55], is utilized for training. To prevent overfitting and boost the model's accuracy, a regularization term of $\lambda = 1 \times 10^{-4}$ is added to the loss function described by

$$L_{MSE} = \frac{1}{m}\sum\left(\hat{Y} - Y\right)^2 + \frac{\lambda}{2m}\sum\|W\|_F^2 \tag{9}$$

where $\hat{Y}$ is the energy predicted by the network, Y is the energy from DFT, m is the number of training points, and $|W\|$ is the Frobenius norm of all the weights and biases of the neural networks. The output layer will always consist of one node that represents the energy of a particular atom. More information on the RANN formalism can be found in the works of Dickel et al. [37] and Nitol et al. [45]. Details on the metaparameters and network architecture used for the RANN Ti-Al potential can be found in Section 3.1. The LAMMPS implementation of RANN can be found at https://github.com/ranndip/ML-RANN (accessed on 11 November 2024).

2.3. Generalized Stacking Fault Energies

When validating the generalized stacking fault energies (GSFEs), we focus on the basal and prismatic slip systems for the α and $D0_{19}$ phases, the pyramidal I and pyramidal II slip

systems for the $D0_{19}$ phase, and the $(1\,1\,1)$ plane for the $L1_0$ phase. For the α phase, the GSFE was computed for pure Ti first. Then, one Ti atom was swapped to an Al atom to observe the impact that solute Al has on the GSFE. The structures used to obtain the GSFE curves were created using the atomman (version 1.5.0) Python (version 3.10) package [56,57]. The simulation cells ranged from 20 to 80 atoms depending on structure and orientation. The fault plane was placed approximately in the middle of the cell. Different structures were created by moving the atoms above the fault plane in two independent directions until the original configuration was reached. The structures were then put into a LAMMPS simulation containing periodic boundary conditions in the x and y directions and a free surface normal to the glide plane (z direction). The atoms were allowed to relax in the z direction but could not move in the x or y directions.

2.4. Phase Diagram

The phase diagram simulations are split into two parts: the α-to-$D0_{19}$ transition and the α-to-β transition. The α-to-$D0_{19}$ transition employs the semi-grand-canonical Monte Carlo (MC) [58] method in LAMMPS. The technique used in this work was motivated by the work of Kim et al. [25] Pure α-Ti was equilibrated to the desired temperature and given a chemical potential value (μ). The semi-grand-canonical MC fix in LAMMPS employs the Metropolis acceptance criterion [59] with the addition of a chemical potential difference term, $\Delta\mu$. This fix attempts to swap a Ti atom with an Al atom 10 times for every MD timestep and accepts the swap according to the Metropolis algorithm [59]. More information about the acceptance probability can be found in the work of Sadigh et al. [58]. The simulations consisted of 1024 atoms and were run at varying temperatures for 40 ps. The same was conducted with a $D0_{19}$ structure. By plotting the equilibrated atomic percentage of Al against $\Delta\mu$ for the initial α structure and the $D0_{19}$ structure, a hysteresis loop can be found. The final atomic percentage of Al before the α phase jumps to the $D0_{19}$ phase corresponds to the phase transition point for the α-to-$D0_{19}$ transition. The final atomic percentage of Al before the $D0_{19}$ phase spontaneously becomes the α phase corresponds to the phase transition point of the $D0_{19}$-to-α transition.

The method to obtain the α-to-β phase boundary involved several simulations and was based on the work of Dickel et al. [43]. Simulations were run for Al concentrations from 0% to 20% Al in 2.5% increments. For structures containing Al, MC MD simulations were used to place solute Al in their preferred lattice sites. First, the enthalpy of the α, β, and liquid phases must be found as a function of temperature for varying concentrations of Al. These enthalpies are used in the calculation of the relative Gibbs free energy described later. Next, simulations inducing a solid–liquid interface must be run. The following steps describe simulations for the α–liquid interface; however, the same procedure was used for the β–liquid interface simulations. An α phase simulation cell composed of 27,648 atoms was heated to 1000 K over 5 ps. Half of the cell was then heated over 5 ps to induce an amorphous region. Next, a constant enthalpy calculation (nph) was applied. This allowed the cell to change size in the direction normal to the solid–liquid interface to equilibrate at zero pressure. The equilibrated temperature was considered the melting point. Once this was complete, the Gibbs–Helmholtz relation could be integrated to calculate the relative Gibbs free energy. The Gibbs–Helmholtz relation is defined by

$$\left(\frac{\partial\left(\frac{G(T)}{T}\right)}{\partial T}\right)_p = -\frac{H(T)}{T^2} \tag{10}$$

where the Gibbs free energy and the enthalpy of the system at some temperature, T, are given by $G(T)$ and $H(T)$, respectively. After integration, the relative Gibbs free energy, ΔG,

was found, and the transition temperature between the α and β phases was taken to be the temperature at which $\Delta G = 0$.

3. Results

3.1. Potential Creation

Figure 1 illustrates the development of the RANN potential using a multilayer perceptron artificial neural network, adapted from the methods described by Dickel et al. [37]. The previously mentioned DFT database used to train the potential includes a total of 62,724 simulations and 2,830,192 unique atomic environments. Each fingerprint used in the creation of the RANN potential contains metaparameters that can be adjusted to improve accuracy. Once the desired accuracy is achieved, the new potential undergoes primary validation. Primary validation includes checking the lattice parameter, elastic constants, ground-state structure, etc., against the values given by DFT to ensure that the potential has properly trained over the DFT database. If any of the tests yield incorrect results, new DFT data can be generated to inform the network of any missing information. Once the potential passes primary validation, it is tested for its prediction capability by repeating basic validation tests at finite temperatures, calculating GSFEs, and calculating phase boundaries. If the potential fails to give accurate predictions compared to experimental values, new DFT data can be generated to inform the network, and the cycle begins again. This new DFT data should not include data used for prediction. Rather, it should include more random perturbations of different phases, more amorphous structures, etc. Potential prediction should be a test of the potential's capabilities and not a training objective. The potential used in this work was chosen after tuning the metaparameters to achieve accuracy within 5.0 meV/atom. The Ti-Al RANN potential can be found at https://github.com/ranndip/RANN-potentials/blob/main/TiAl.nn (accessed on 15 November 2024).

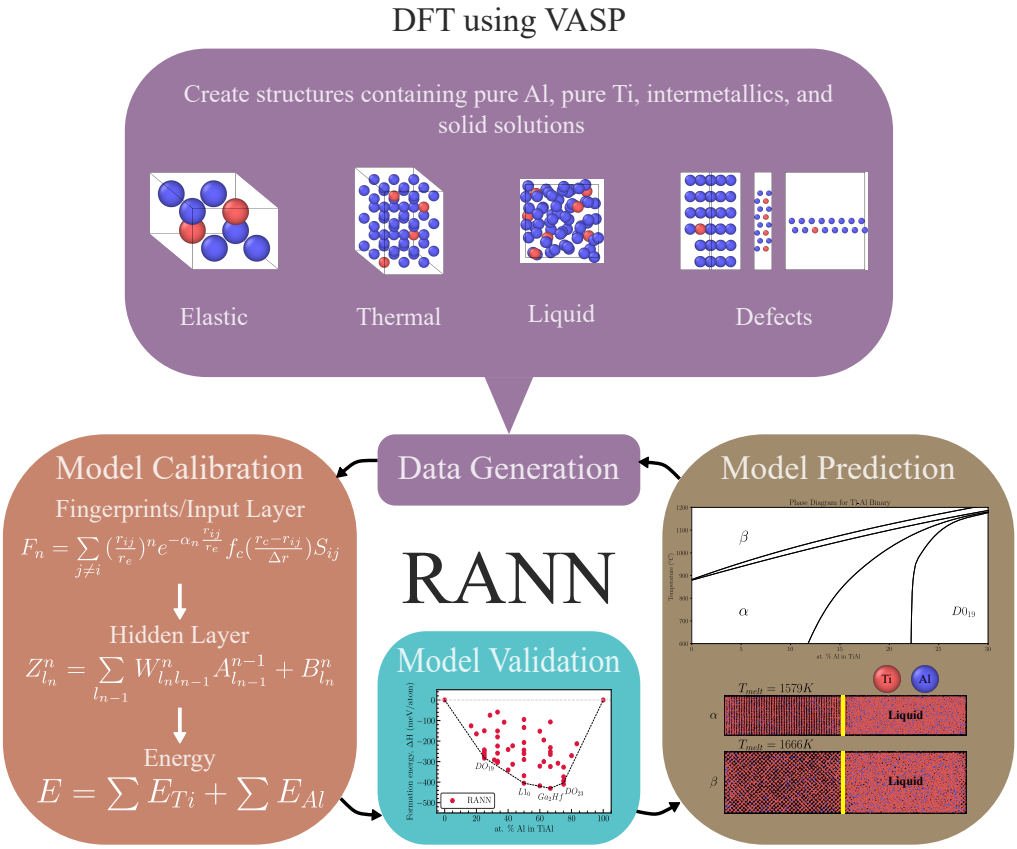


Figure 1. Summary of the RANN potential development workflow.

The RANN potential incorporates two neural networks—one for Ti and one for Al. Both networks employ one hidden layer. Metaparameters for both networks can be seen in Table 1. The r_e term represents the nearest neighbor distance in the ground-state structure for the specified atom type's network. The HCP structure is used for the Ti network, and the FCC structure is used for the Al network. r_c is the cutoff radius and is chosen to capture a wide range of interactions while maintaining computational efficiency. Δr determines the width of the cutoff transition and is taken to be $r_c - r_e$. As in MEAM, α is calculated using $(9B_0\Omega_0/E_c)^{1/2}$, where B_0 is the bulk modulus, Ω_0 is the equilibrium atomic volume of the ground-state structure, and E_c is the cohesive energy. m, n, and β_k are all chosen to balance accuracy with computational efficiency and take into account the metaparameters used in previous works [37,44,46,47]. The Ti network architecture is explicitly defined as $58 \times 26 \times 1$, where 58 describes the number of neurons created by the structural fingerprints in the input layer, 26 describes the number of neurons in the hidden layer, and 1 describes the output neuron that gives the atomic energy. The input layer for the Ti network is created from two pair interaction fingerprints described by Equation (1) and two three-body interaction fingerprints described by Equation (2). The first pair interaction describes the Ti-Ti interaction and contributes five neurons to the input layer by creating a neuron for each n $\in \{-1 \ldots 3\}$. This fingerprint calculates a value for the Ti atom, i, by summing over all of its neighbors, j, only if atom j is of type Ti. The second pair interaction describes the Ti-Al interaction and also contributes five neurons to the input layer by giving a neuron for each n$\in \{-1 \ldots 3\}$. The first three-body fingerprint in the Ti network describes the Ti-Ti-Ti interaction. This fingerprint accounts for 24 neurons in the input layer by calculating a value for each unique pairing of m and β_k in the Ti column of Table 1. In order for the Ti-Ti-Ti three-body fingerprint to sum over the neighboring atoms j and k, atoms i, j, and k must be Ti atoms. The final three-body fingerprint used in the Ti network describes the Ti-Al-All interaction, where All can be either a Ti atom or an Al atom. The Ti-Al-All three-body fingerprint also contributes 24 neurons to the input layer for the same reason as the previous three-body fingerprint. The Al network architecture is defined as $50 \times 22 \times 1$, where 50 is the number of neurons from the structural fingerprints in the input layer, 22 is the number of neurons in the hidden layer, and 1 is the atomic energy given by a single neuron in the output layer. Fingerprints used in the Al network include an Al-Al pair interaction fingerprint, an Al-Ti pair interaction fingerprint, an Al-Al-Al three-body fingerprint, and an Al-Ti-All three-body fingerprint. The Al-Al pair fingerprint and the Al-Ti pair fingerprint contribute five neurons each to the input layer of the Al network, as a neuron is created using Equation (1) for each n $\in \{-1 \ldots 3\}$. The Al-Al-Al three-body fingerprint and the Al-Ti-All fingerprint account for 20 input neurons each by calculating Equation (2) for each unique pairing of m and β_k in the Al column of Table 1. The size of each network's hidden layer is chosen with previous works [37,44,46,47] in mind to keep the desired level of accuracy while also retaining computational efficiency.

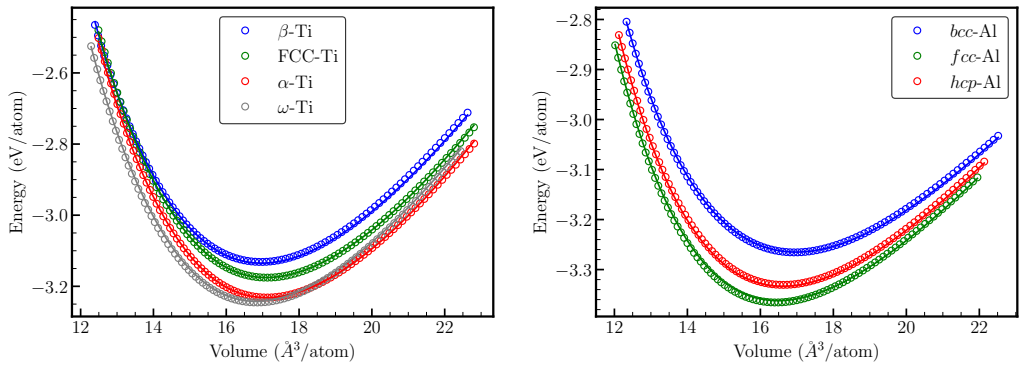
The network's performance is evaluated by aggregating the outputs for all atoms in a simulation and comparing these results with total energies derived from DFT calculations. The mean square error (MSE) is calculated and employed as the loss function, which is minimized to refine the weights and biases. Post-training, the MSE for the training and validation datasets are recorded at 4.68 meV/atom and 4.98 meV/atom, respectively, for the Ti-Al dataset. The high validation accuracy highlights the model's reliability and indicates that the potential is likely able to reproduce structures contained in the dataset within a 4.98 meV/atom margin of error.

Table 1. Metaparameters for Ti and Al.

Fingerprint Metaparameters	Ti	Al
m	$\in \{0 \ldots 5\}$	$\in \{0 \ldots 4\}$
n	$\in \{-1 \ldots 3\}$	$\in \{-1 \ldots 3\}$
r_e (Å)	2.924308	2.856975
α	4.72	4.685598
β_k	1, 2, 5, 9	1, 2, 5, 9
r_c (Å)	8.0	8.0
Δr (Å)	5.075692	5.143025
C_{min}	0.49	0.49
C_{max}	1.44	1.44

3.2. Primary Validation

The primary validation of the RANN Ti-Al potential is a measure of how well the potential performs on data that is included in the training database. Figure 2 shows an energy vs. volume curve for α, β, ω, and FCC phases in pure Ti as well as FCC, BCC, and HCP phases in pure Al. RANN predicts the α and ω phases to be the low-energy structures in pure Ti, in agreement with DFT results. In pure Al, RANN follows DFT in predicting the FCC phase to be the lowest-energy phase.

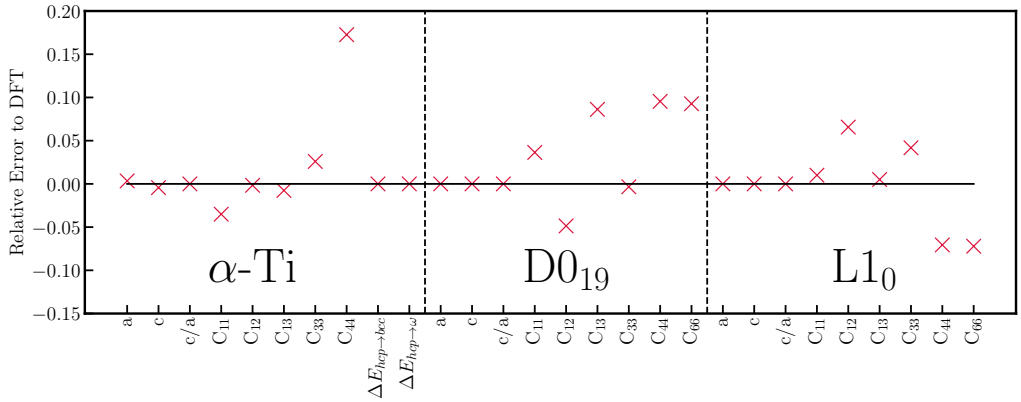


(**a**) Ti (**b**) Al

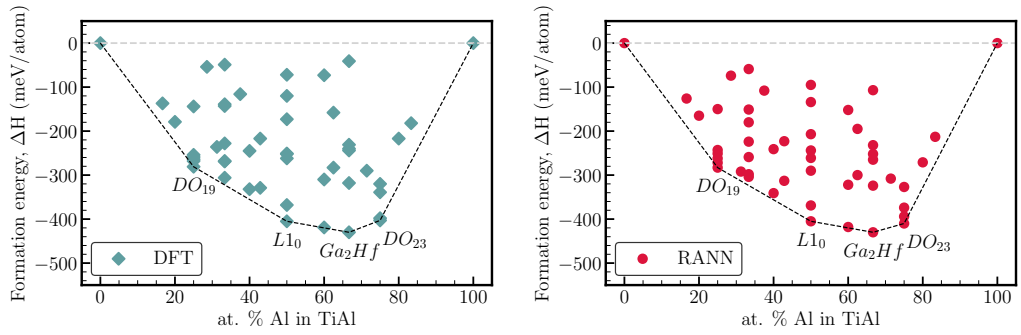
Figure 2. EV curves for (**a**) Ti and (**b**) Al. Circles represent DFT and lines represent RANN.

Figure 3 shows the lattice parameters and elastic constants for pure α-Ti, $D0_{19}$, and $L1_0$ phases as well as the convex hull for RANN compared to DFT. RANN is in good agreement with DFT calculations. The C_{44} elastic constant for α-Ti deviates the furthest from DFT at 17%; however, the average deviation across these properties is 1.4%. Kiely et al. [60] show that elastic constants calculated from DFT are consistently within 15% of experimental values, and Jafari et al. [61] show that calculated elastic constants can vary by 10% by altering DFT methods. Nitol et al. [47] demonstrate that the change in energy as a function of strain for DFT shows anharmonicity and represents a temperature dependence. This temperature dependence indicates that the elastic constants predicted by RANN should become closer to those of DFT at finite temperatures. Although the α-Ti C_{44} elastic constant shows a relatively high error compared to DFT, the relative error between the RANN potential and the experimental value (50.8 GPa [62]) is -6%. Considering the many sources of fluctuation as well as the fact the RANN potential predicts the α-Ti C_{44} elastic constant to be between that of DFT and the experiment, the relative error between the RANN potential and DFT does not represent a source of concern. Both RANN and DFT show that the $D0_{19}$, $L1_0$, Ga_2Hf, and $D0_{23}$ structures are the low-energy structures with increasing Al

concentration. The $D0_{22}$ structure, which is seen experimentally, has a formation energy 5 meV/atom and 6 meV/atom higher than the $D0_{23}$ structure for DFT and the RANN potential, respectively. In order for the potential to accurately model the Ti-Al system, it must show that Al is soluble in Ti. DFT shows the substitutional energy of Al in Ti for the stable α phase to be −829 meV. RANN shows the substitutional energy to be −849 meV; therefore, RANN correctly predicts Al to be soluble in Ti. While this work focuses on the Ti-Al system with up to 30 at.% Al concentration, Figure 4 shows the lattice and elastic constants for the $D0_{22}$ and $TiAl_2$ (Ga_2Hf) structures. The largest error for both structures occurs for the C_{13} elastic constant at 23% for the $D0_{22}$ structure and 25% for the $TiAl_2$ structure. Augmenting the training database with more information on these structures could drive these errors down and extend the use case for this potential. More information on the material properties for various phases can be found in the Supplemental Information (see also references [14,17,29,44,62–64,64–87] therein).



(**a**) Relative error for RANN compared to DFT



(**b**) Convex hull for DFT (**c**) Convex hull for RANN

Figure 3. (**a**) Relative error for the RANN Ti-Al potential compared to DFT for the α-Ti, $D0_{19}$, and $L1_0$ phases. (**b**) Convex hull for DFT and (**c**) RANN Ti-Al potential.

Predicting the forces acting on individual atoms can be an indicator of how well an atomic potential will succeed in accurately displaying results for dynamic simulations. Here, the x, y, and z components of the force acting on individual atoms for finite-temperature perturbations of α-Ti, β-Ti, and ω-Ti structures are computed using DFT as well as with the RANN potential. While possible to train potentials over forces and energies from DFT, the RANN potential created in this work only trains over atomic energies. Shown in Figure 5, RANN shows an MSE of 0.12 eV/Å, 0.11 eV/Å, and 0.17 eV/Å for α-Ti, β-Ti, and ω-Ti, respectively.

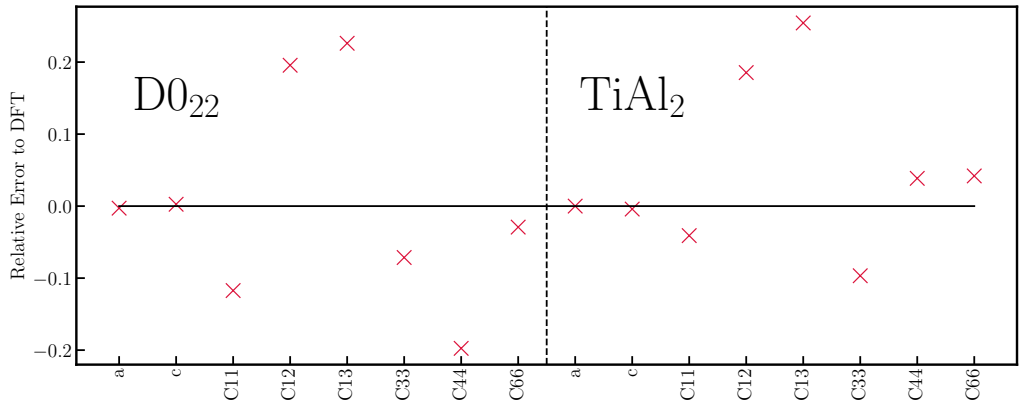
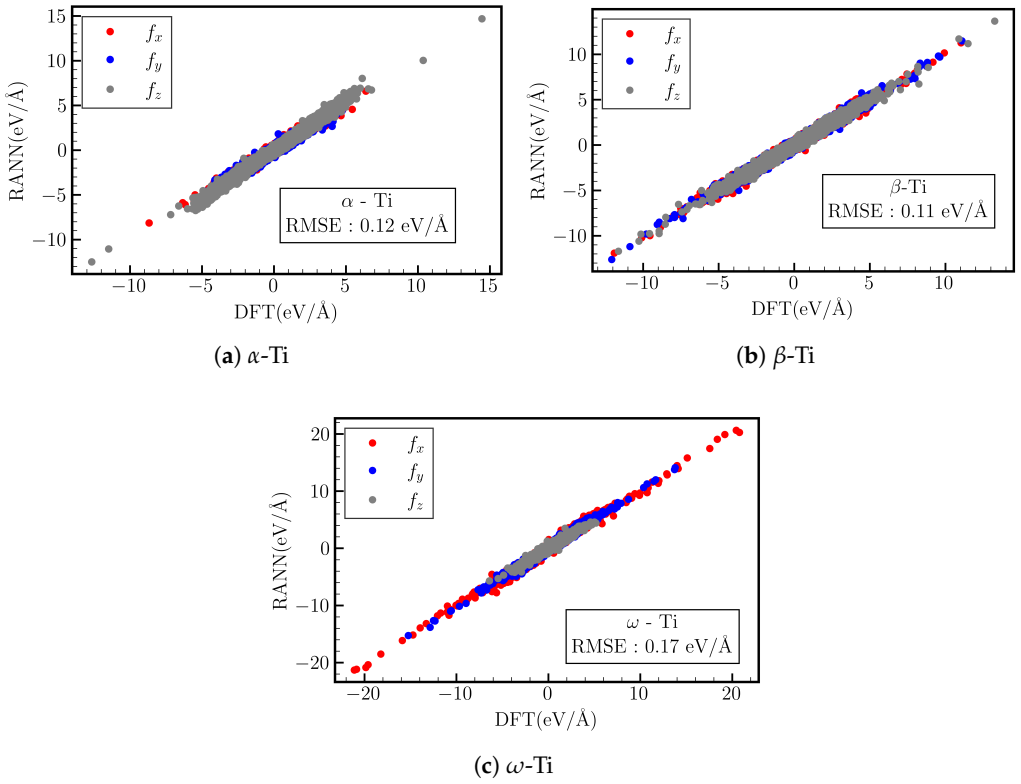


Figure 4. Relative error for RANN compared to DFT. DFT values for the $D0_{22}$ structure adapted from Ref. [88], and DFT values for the Ga_2Hf $TiAl_2$ structure are adapted from Ref. [89].



(**a**) α-Ti (**b**) β-Ti

(**c**) ω-Ti

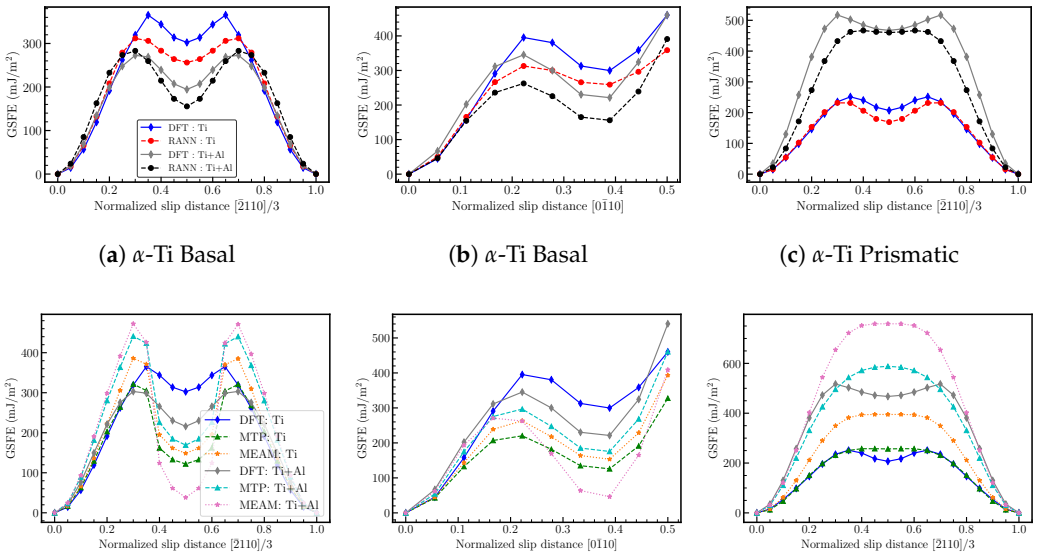
Figure 5. Force comparison for randomly perturbed (**a**) α-Ti, (**b**) β-Ti, and (**c**) ω-Ti supercells. The y-axes represent the RANN Ti-Al potential, and the x-axes represent DFT. A line along $y = x$ indicates that the RANN Ti-Al potential predicts the same force as DFT.

3.3. GSFE Validation

The presence of solute atoms along glide planes can significantly influence dislocation mechanisms. This is vital because dislocations are the main vectors of plastic deformation in metals. By understanding the interaction between solutes and dislocations, we can better predict and manage the mechanical properties of alloys. Previous studies, such as those using generalized stacking fault energy (GSFE) calculations, have demonstrated how these interactions can enhance properties like strength, ductility, and toughness [90]. For instance, specific solute atoms may obstruct dislocation movement, contributing to solid solution strengthening. In Ti-Al alloys, Al solutes disrupt the emission of prismatic dislocations and alter the energy of basal/prismatic faults. This effect helps to stabilize

the immobile, non-planar core of screw $1/3\langle 1\,1\,\bar{2}\,0\rangle$ dislocations, significantly enhancing the strength of α-Ti [91]. Understanding GSFE and the influence of solute positioning allows for the tailoring of alloy compositions to achieve desired mechanical traits, crucial for designing alloys for specific applications requiring high strength or improved ductility. Comparing the GSFE predicted by the RANN Ti-Al potential to the GSFE produced by DFT gives insight into the potential's ability to accurately simulate plasticity. It should be noted that while the RANN potential is compared to DFT data, this DFT data is not in the training database.

The RANN Ti-Al potential is in good agreement with DFT for both the pure Ti case and when solute Al is adjacent to the glide plane. The RANN Ti-Al potential shows softening in the basal plane when Al is near the glide plane, as expected. The MEAM [25] potential also shows a softening in the basal plane with the addition of a solute Al atom, but it severely underestimates the GSFE for both pure Ti and α-Ti. The MTP [41] displays a stiffening in the basal plane with the addition of a solute Al atom. This is problematic, as the presence of Al is known to cause solution strengthening through a decrease in stacking fault energy [7]. The RANN, MEAM, and MTP Ti-Al potentials all agree with the DFT results in showing a stiffening in the prismatic plane after an Al atom is placed adjacent to the glide plane. While both the MEAM and MTP Ti-Al potentials agree with the DFT values, the MEAM Ti-Al potential overestimates the GSFE in the prismatic plane. Figure 6 shows the GSFE for the mentioned planes.

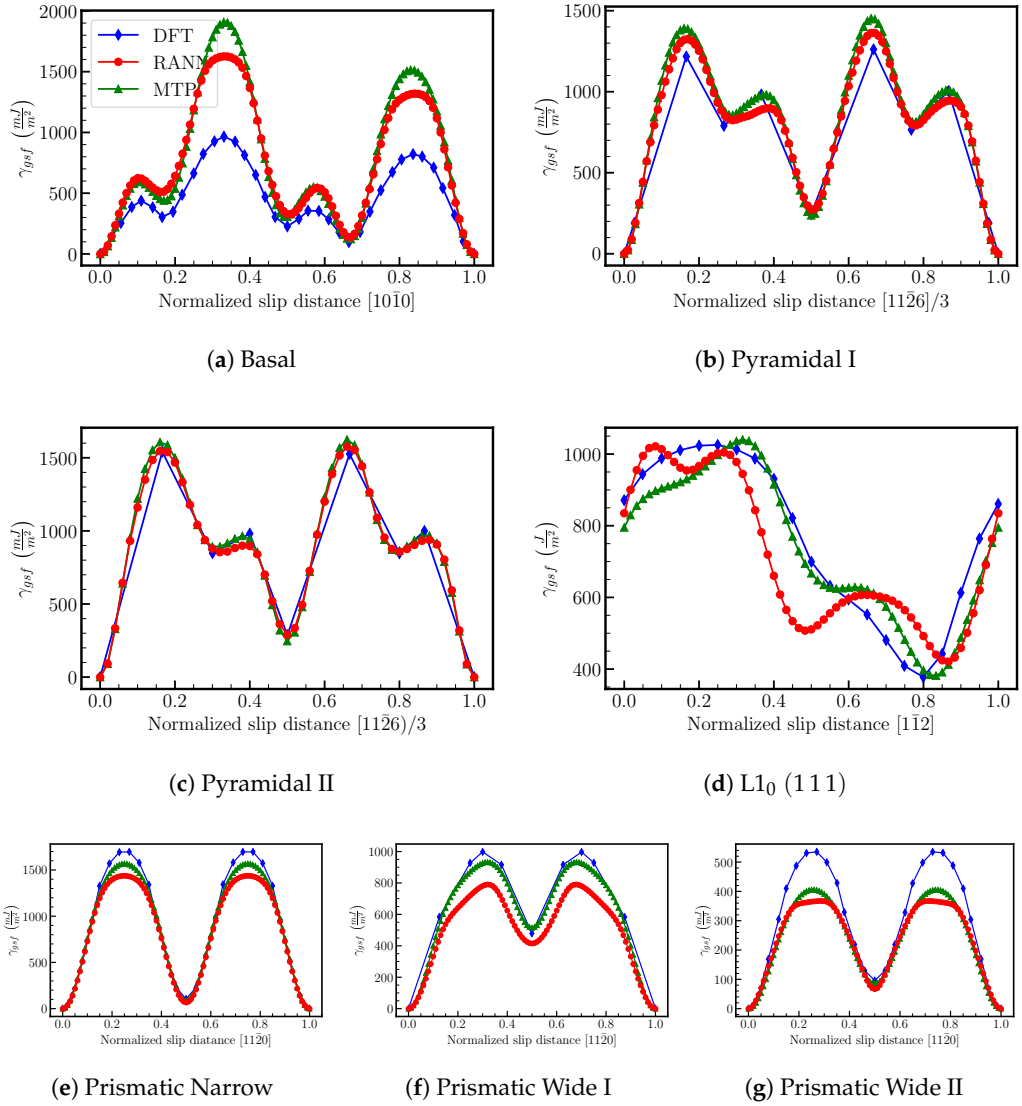


(**a**) α-Ti Basal (**b**) α-Ti Basal (**c**) α-Ti Prismatic

(**d**) α-Ti Basal (**e**) α-Ti Basal (**f**) α-Ti Prismatic

Figure 6. GSFE of Ti-Al alloy, where solute Al is in the first nearest position relative to the glide plane for the (**a**,**b**,**d**,**e**) basal and (**c**,**f**) prismatic planes.

The GSFE was also calculated for several planes in the formed intermetallic phases. The basal, pyramidal I, pyramidal II, prismatic narrow, prismatic wide I, and prismatic wide II planes were examined for the $D0_{19}$ phase, and the $(1\,1\,1)$ plane was examined for the $L1_0$ phase. The MTP is very accurate in predicting the GSFE for intermetallics [41]. Shown in Figure 7, RANN is found to be in agreement with the GSFE predicted by the MTP for intermetallic structures.



(**a**) Basal (**b**) Pyramidal I

(**c**) Pyramidal II (**d**) $L1_0$ $(1\,1\,1)$

(**e**) Prismatic Narrow (**f**) Prismatic Wide I (**g**) Prismatic Wide II

Figure 7. GSFE given by the RANN Ti-Al potential, MTP Ti-Al potential, and DFT for the $D0_{19}$ (**a**) basal, (**b**) pyramidal I, (**c**) pyramidal II, (**d**) $L1_0$ $(1\,1\,1)$, (**e**) prismatic narrow, (**f**) prismatic wide I, (**g**) prismatic wide II planes. DFT data adapted from Ref. [41].

3.4. Potential Prediction at Finite Temperature

Being able to accurately model the Ti-Al system at finite temperatures and with varying concentrations of Al is very important. A potential must accurately display fundamental material properties with varying concentrations of Al as well as predict at what temperature or Al concentration phase changes will occur. The RANN, MTP [41], and MEAM [25] Ti-Al potentials are capable of predicting the lattice constants for both pure Ti as a function of temperature and Ti-Al alloys as a function of varying Al concentration, in agreement with the experimental works of Spreadborough and Christian [92], Kornilov et al. [93], and Rostoker [94]. Lattice constants for pure Ti as a function of temperature can be found in Figure 8.

The MTP and MEAM slightly overestimate the lattice parameter along the *a*-axis at low temperatures; however, the MTP approaches experimental results as temperature increases. Although the RANN Ti-Al potential follows the trend of experimental results for the *a*-axis, it underestimates the lattice parameter. For the *c*-axis, MEAM overestimates the lattice parameter, while both the RANN Ti-Al potential and MTP underestimate it. The RANN Ti-Al potential's propensity to underestimate the lattice parameters can be attributed to the

fact that the DFT data used in the training database gives lower lattice constants than that of experimental data. More information along with a comparison between experimental data, DFT, and the RANN Ti-Al potential can be found in the Supplemental Information. While the RANN Ti-Al potential underestimates the lattice constants, it produces a c/a ratio closer to experimental data than the other potentials tested. This can be seen in Figure 9.

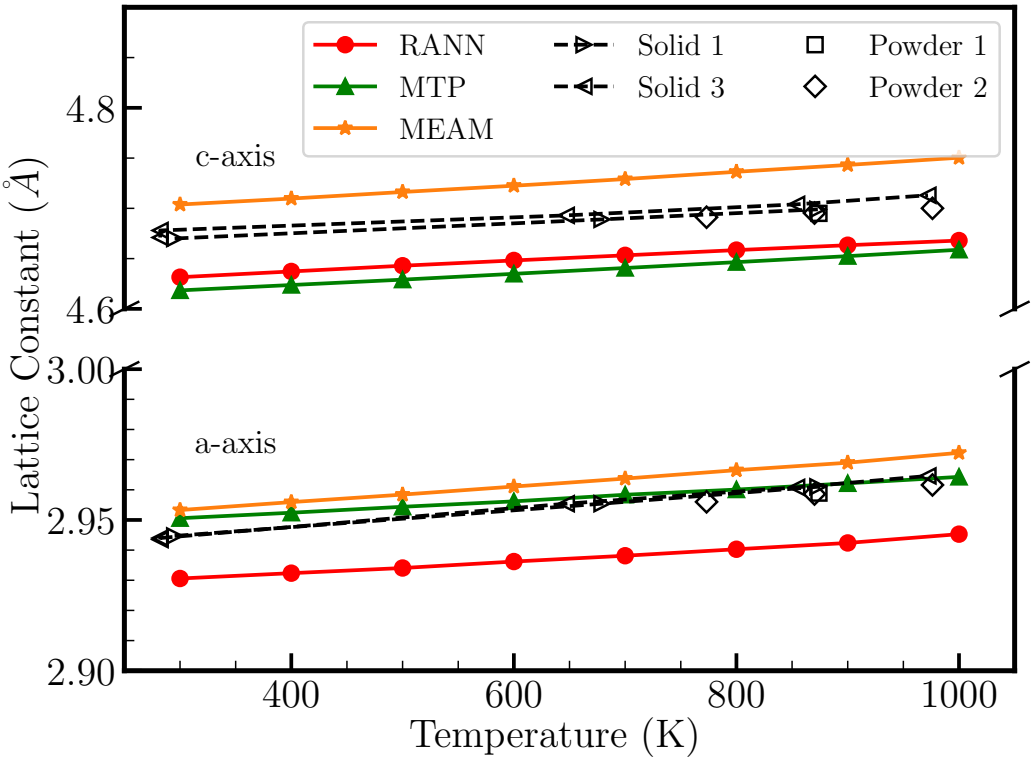


Figure 8. Lattice constants for the *a*- and *c*-axes for pure Ti as a function of temperature calculated with the RANN Ti-Al potential, MTP, MEAM, and experimental dataExperimental data adapted from Ref. [92].

Lattice constants with varying aluminum concentration at 300 K for RANN, MTP, MEAM, and experimental results can be seen in Figure 10. The MTP and MEAM Ti-Al potentials agree with experimental findings for the *a*-axis, and the MEAM Ti-Al potential agrees with experimental findings for the *c*-axis as well. Both the RANN and MTP Ti-Al potentials approach the experimental results for the *c*-axis with increasing Al concentration, with the RANN potential approaching first. The RANN potential replicates the experimental trend for the *a*-axis with values approximately 0.2 Å lower than the experimental data.

The RANN potential is capable of reproducing the phase diagram with up to 30% Al. The $D0_{19}$-to-α transition predicted by RANN is comparable to that of CALPHAD as well as previous work performed by Kim et al. [25]. Simulations for this transition were run from 900 K to 1200 K in 100 K increments. The hysteresis loop becomes too small to accurately measure where the phase transition occurs at temperatures higher than 1200 K for the RANN Ti-Al potential and at temperatures higher than 1100 K for the MTP potential. Figure 11 shows one of the hysteresis loops found using the RANN Ti-Al potential. The Al concentrations at which each potential predicts the phase transitions from α to $D0_{19}$ and from $D0_{19}$ to α can be found in Table 2.

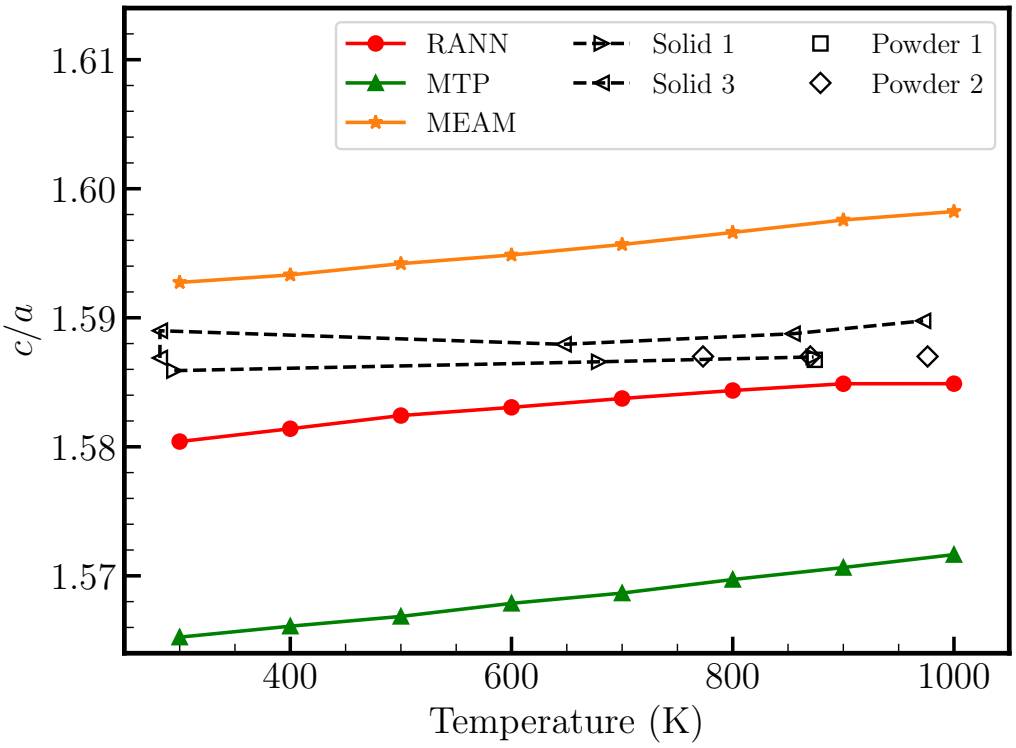


Figure 9. c/a ratio for pure Ti as a function of temperature calculated by the RANN Ti-Al potential, MTP, MEAM, and experimental values adapted from Ref. [92].

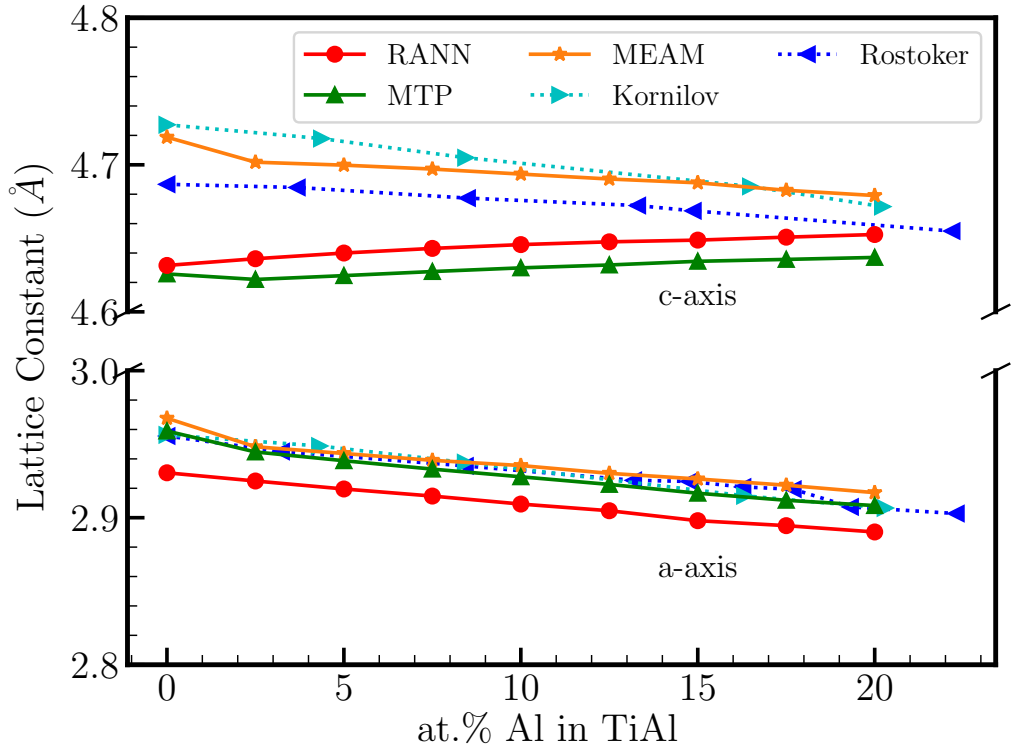


Figure 10. Lattice constant as a function of Al concentration at 300 K for RANN, MTP, MEAM, and experimental values. Experimental values adapted from Refs. [93,94].

Table 2. at.% Al at which RANN, MTP [41], and MEAM [25] predict the α-to-D0$_{19}$ and D0$_{19}$-to-α phase transitions at multiple temperatures.

$T(K)$	$\alpha \rightarrow D0_{19}$ $(at.\%\ Al)$		D0$_{19}\rightarrow\alpha$ $(at.\%\ Al)$		$T(K)$	$\alpha \rightarrow D0_{19}$ $(at.\%\ Al)$	D0$_{19}\rightarrow\alpha$ $(at.\%\ Al)$
	RANN	**MTP**	**RANN**	**MTP**		**MEAM**	**MEAM**
900	8.6	12.9	22.7	23.6	973	6.3	24.1
1000	9.7	15.2	22.3	23.4	1023	8.7	24.1
1100	11.1	18.2	21.6	23.7	1123	13.3	23.8
1200	14.2	—	22.2	—	1173	16.9	23.2

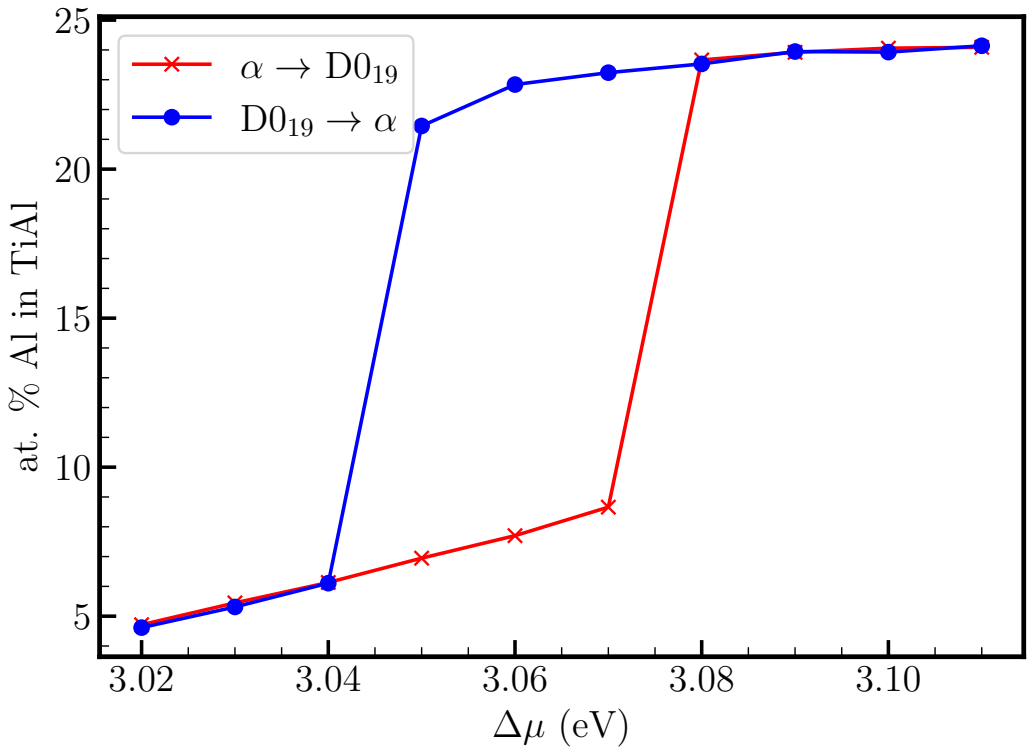


Figure 11. Hysteresis loop from semi-grand-canonical Monte Carlo simulations at 900 K. Atomic percentages for phase boundaries are taken as the last data point given before the spontaneous phase change.

While the RANN Ti-Al potential slightly underestimates the α-to-D0$_{19}$ phase transition compared to CALPHAD, the MTP Ti-Al potential slightly overestimates it. The MTP also overestimates the D0$_{19}$-to-α+D0$_{19}$ phase boundary, but the RANN Ti-Al potential shows good agreement with CALPHAD. The MEAM [25] Ti-Al potential displays an accurate transition between α and D0$_{19}$ at higher temperatures. At lower temperatures, MEAM predicts that the phase boundary going from the α phase to the D0$_{19}$ phase occurs at Al concentrations lower than RANN, MTP, and CALPHAD.

To the best of the authors' knowledge, no existing interatomic potential exists that accurately shows Al as an α-stabilizer in Ti-Al alloys by reproducing the α-to-β transition. The ability to model this phase transition is of great importance, as many commercially available Ti-Al alloys contain two-phase regions composed of the α and β phases in order to increase strength and creep resistance [95]. Additionally, the β phase is known to increase the workability of Ti alloys [9]. Figure 12 displays the solid–liquid interface for the α and β phases at 10% Al concentration as well as the transition temperature for 0%, 10%, and 20% Al concentrations. Images used for the solid–liquid interface were taken from Ovito [96].

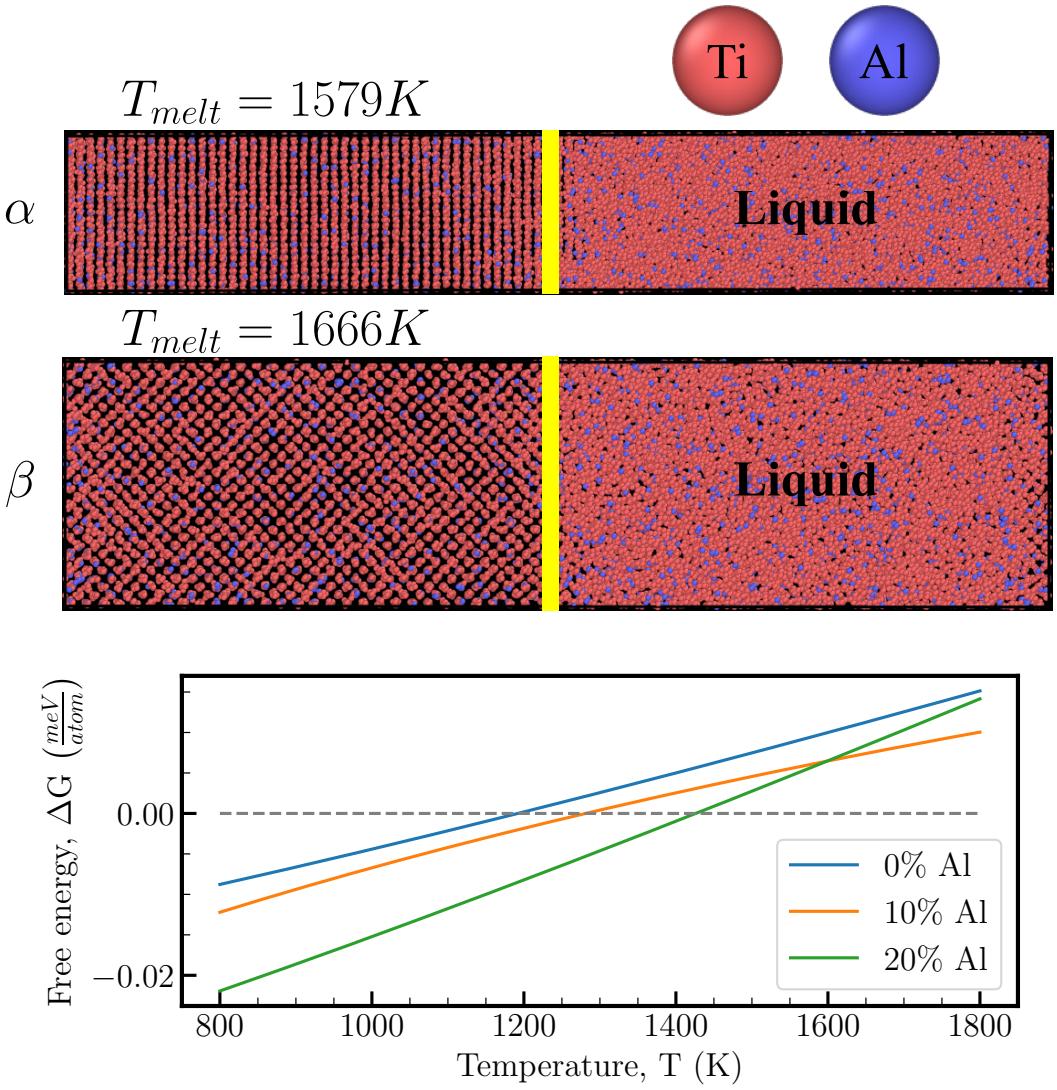


Figure 12. Top: Simulation cell with a solid–liquid interface for the α (top) and β (middle) phases for 10% Al concentration. The left side of each simulation cell contains an ordered crystal structure, the right side of each cell shows the heated region of amorphous liquid, and the yellow bar on each cell represents the solid–liquid interface [96]. Bottom: Gibbs free energy calculation for 0%, 10%, and 20% Al concentrations. The transition temperature is taken where $\Delta G = 0$.

The transition temperatures were calculated for Al concentrations ranging from 0% Al to 20% Al in 2.5% increments. Table 3 shows the melt temperatures for the α and β phases used for the Gibbs free energy calculation as well as the α-to-β transition temperature calculated using the RANN Ti-Al potential and the MTP.

The values produced by the RANN Ti-Al potential show a clear trend of increasing transition temperature with increasing Al concentration, as is expected when adding an α-stabilizer such as Al. The MTP [41] also shows that Al is an α-stabilizer in Ti; however, the MTP Ti-Al potential does not accurately predict the phase boundary between the α and β phases. The MTP data gives a much steeper slope with increasing Al concentration than that of CALPHAD. The phase boundaries predicted by the interatomic potentials can be seen in Figure 13.

Table 3. Melting temperatures used for calculation of the Gibbs relative free energy and α-β transition temperatures found from the Gibbs relative free energy.

at.% Al	T^{α}_{melt} (K)		T^{β}_{melt} (K)		$T^{\alpha-\beta}_{transition}$ (K)	
	RANN	MTP	RANN	MTP	RANN	MTP
0	1525	1602	1657	1883	1192	1027
2.5	1522	1617	1673	1884	1206	1105
5	1535	1617	1675	1877	1235	1135
7.5	1561	1661	1691	1887	1247	1242
10	1579	1690	1666	1883	1280	1364
12.5	1592	1707	1700	1898	1327	1379
15	1619	1732	1707	1887	1362	1497
17.5	1620	1748	1718	1887	1417	1535
20	1634	1770	1738	1887	1426	1573

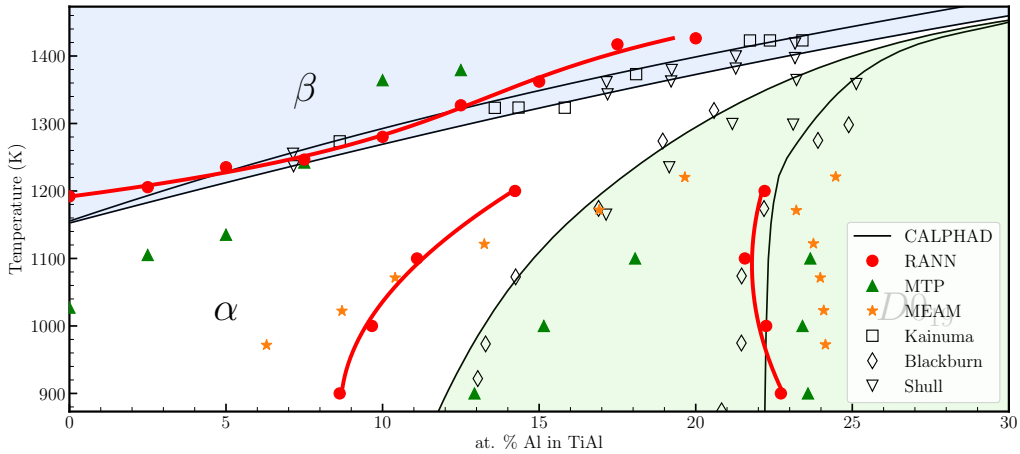


Figure 13. Phase diagram of Ti-Al binary system predicted by RANN, MTP, and MEAM compared to CALPHAD, experimental results adapted from Refs. [97–99]. The line between RANN data points is a cubic spline with an applied smoothing factor to indicate the trend of the data.

The experimental work performed by Kainuma et al. [97], Blackburn [98], and Shull et al. [99] shows good agreement with the phase diagram from CALPHAD. More recently, Ohnuma et al. [100] show that oxygen contamination can cause inaccuracies in the high-temperature phase boundaries of the Ti-Al system; however, their calculated and experimental results show good agreement with the CALPHAD and experimental results shown in Figure 13. The RANN Ti-Al shows sufficient agreement with all of the experimental and CALPHAD data for each phase boundary. While the RANN potential slightly underestimates the α-to-$\alpha + D0_{19}$ phase boundary, it correctly matches the trends shown. The RANN potential shows very good agreement with the work of Blackburn [98] for the $D0_{19}$-to-$\alpha + D0_{19}$ phase boundary. For the α-to-β transition, the RANN potential follows the trend of the experimental results as well as the CALPHAD calculation.

4. Discussion

The microstructure of Ti-Al alloys plays a key role in determining material properties. Previous attempts at modeling the Ti-Al system have been limited to only capturing solid solutions or formed intermetallics—not both. The RANN potential presented in this work bridges the gap between the currently available classical and ML potentials for the Ti-Al binary system. Classical potentials such as the MEAM potential introduced by Kim et al. [25] accurately model basic properties for solid solutions and formed intermetallic structures; however, they fail to capture accurate GSFEs and elastic constants for formed

intermetallics. MEAM [25] also does not report on the α-β phase boundary. The MTP produced by Qi et al. [41] is promising for basic properties and plastic properties for formed intermetallic structures; however, it does not give accurate results for solid solutions. The Ti-Al RANN potential gives basic properties and GSFEs in agreement with DFT and phase boundaries in agreement with CALPHAD. The lattice constants and elastic constants predicted by RANN show an average deviation of 3.33% from DFT, with the largest deviation coming from the C_{44} elastic constant for α-Ti. DFT shows a decrease in GSFE compared to α-Ti when adding an Al atom adjacent to the glide plane. RANN accurately displays this trend as well. RANN mimics the slope of the phase boundaries between α and β as well as α and $D0_{19}$ given by CALPHAD. The α-to-$D0_{19}$ phase boundary predicted by RANN occurs at an Al concentration roughly 3% lower than that of CALPHAD; however the $D0_{19}$-to-α phase boundary given from RANN is within approximately 1% of CALPHAD. As the temperature increases in systems with an Al concentration near the α-to-$D0_{19}$ phase boundary, RANN correctly predicts that the α phase becomes more stable than the two-phase region containing α and $D0_{19}$. RANN shows the α-β boundary to be along the upper phase boundary given by CALPHAD. This shows that the RANN potential accurately finds Al to be an α-stabilizer when added to Ti. These results show that RANN is capable of modeling the phase behaviors, solute effects, and thermomechanical properties of Ti-Al systems with up to 30% Al concentration.

Supplementary Materials: The following supporting information can be downloaded at https://www.mdpi.com/article/10.3390/met16020140/s1.

Author Contributions: Conceptualization, M.S.N.; Methodology, M.N. and M.S.N.; Software, M.N. and M.S.N.; Validation, M.N. and M.S.N.; Formal analysis, M.N.; Investigation, M.N. and M.S.N.; Resources, M.N., M.S.N. and S.J.F.; Data curation, M.N.; Writing—original draft, M.N. and M.S.N.; Writing—review & editing, M.N., C.D.B. and D.E.D.; Visualization, M.N. and M.S.N.; Supervision, M.S.N., S.J.F., C.D.B. and D.E.D.; Project administration, M.S.N., S.J.F., C.D.B. and D.E.D.; Funding acquisition, S.J.F. All authors have read and agreed to the published version of the manuscript.

Funding: This research received no external funding.

Data Availability Statement: The original contributions presented in this study are included in the article/Supplementary Material. Further inquiries can be directed to the corresponding author.

Conflicts of Interest: The authors declare no conflict of interest.

References

1. Appel, F.; Paul, J.D.H.; Oehring, M. *Gamma Titanium Aluminide Alloys: Science and Technology*; John Wiley & Sons: Hoboken, NJ, USA, 2011.
2. Clemens, H.; Mayer, S. Intermetallic titanium aluminides in aerospace applications–processing, microstructure and properties. *Mater. High Temp.* **2016**, *33*, 560–570. [CrossRef]
3. Leyens, C.; Peters, M. *Titanium and Titanium Alloys: Fundamentals and Applications*; Wiley Online Library: Hoboken, NJ, USA, 2006.
4. Dimiduk, D. Gamma titanium aluminide alloys—an assessment within the competition of aerospace structural materials. *Mater. Sci. Eng. A* **1999**, *263*, 281–288. [CrossRef]
5. Kim, S.W.; Na, Y.S.; Yeom, J.T.; Kim, S.E.; Choi, Y.S. An in-situ transmission electron microscopy study on room temperature ductility of TiAl alloys with fully lamellar microstructure. *Mater. Sci. Eng. A* **2014**, *589*, 140–145. [CrossRef]
6. Palomares-García, A.J.; Pérez-Prado, M.T.; Molina-Aldareguia, J.M. Effect of lamellar orientation on the strength and operating deformation mechanisms of fully lamellar TiAl alloys determined by micropillar compression. *Acta Mater.* **2017**, *123*, 102–114. [CrossRef]
7. Guo, Z.; Miodownik, A.; Saunders, N.; Schillé, J.P. Influence of stacking-fault energy on high temperature creep of alpha titanium alloys. *Scr. Mater.* **2006**, *54*, 2175–2178. [CrossRef]
8. Appel, F.; Wagner, R. Microstructure and deformation of two-phase γ-titanium aluminides. *Mater. Sci. Eng. Rep.* **1998**, *22*, 187–268. [CrossRef]

9. Veiga, C.; Davim, J.P.; Loureiro, A. Properties and applications of titanium alloys: A brief review. *Rev. Adv. Mater. Sci.* **2012**, *32*, 133–148.
10. Jepson, K.; Brown, A.R.; Gray, J. *Effect of Cooling Rate on the Beta Transformation in Titanium–Niobium and Titanium–Aluminium Alloys*; Technical Report; Royal Aircraft Establishment: Farnborough, UK, 1970.
11. Sato, T.; Hukai, S.; Huang, Y.C. The Ms points of binary titanium alloys. *J. Austral. Inst. Met.* **1960**, *5*, 149–153.
12. Asta, M.; de Fontaine, D.; van Schilfgaarde, M.; Sluiter, M.; Methfessel, M. First-principles phase-stability study of fcc alloys in the Ti-Al system. *Phys. Rev. B* **1992**, *46*, 5055. [CrossRef]
13. Shang, S.; Kim, D.; Zacherl, C.; Wang, Y.; Du, Y.; Liu, Z. Effects of alloying elements and temperature on the elastic properties of dilute Ni-base superalloys from first-principles calculations. *J. Appl. Phys.* **2012**, *112*, 053515. [CrossRef]
14. Liu, Y.; Liu, L.; Wang, S.; Ye, H. First-principles study of shear deformation in TiAl and Ti3Al. *Intermetallics* **2007**, *15*, 428–435. [CrossRef]
15. Ding, R.; Li, H.; Hu, D.; Martin, N.; Dixon, M.; Bowen, P. Features of fracture surface in a fully lamellar TiAl-base alloy. *Intermetallics* **2015**, *58*, 36–42. [CrossRef]
16. Yoo, M.; Zou, J.; Fu, C. Mechanistic modeling of deformation and fracture behavior in TiAl and Ti3Al. *Mater. Sci. Eng. A* **1995**, *192*, 14–23. [CrossRef]
17. Fu, C.; Yoo, M. Elastic constants, fault energies, and dislocation reactions in TiAl: A first-principles total-energy investigation. *Philos. Mag. Lett.* **1990**, *62*, 159–165. [CrossRef]
18. Sun, J.; Trimby, P.; Si, X.; Liao, X.; Tao, N.; Wang, J. Nano twins in ultrafine-grained Ti processed by dynamic plastic deformation. *Scr. Mater.* **2013**, *68*, 475–478. [CrossRef]
19. Lee, T.; Kim, S.W.; Kim, J.Y.; Ko, W.S.; Ryu, S. First-principles study of the ternary effects on the plasticity of γ-TiAl crystals. *Sci. Rep.* **2020**, *10*, 21614. [CrossRef]
20. Daw, M.S.; Baskes, M.I. Embedded-atom method: Derivation and application to impurities, surfaces, and other defects in metals. *Phys. Rev. B* **1984**, *29*, 6443. [CrossRef]
21. Farkas, D.; Jones, C. Interatomic potentials for ternary Nb-Ti-Al alloys. *Model. Simul. Mater. Sci. Eng.* **1996**, *4*, 23. [CrossRef]
22. Zope, R.R.; Mishin, Y. Interatomic potentials for atomistic simulations of the Ti-Al system. *Phys. Rev. B* **2003**, *68*, 024102. [CrossRef]
23. Baskes, M. Application of the embedded-atom method to covalent materials: A semiempirical potential for silicon. *Phys. Rev. Lett.* **1987**, *59*, 2666. [CrossRef] [PubMed]
24. Baskes, M.; Nelson, J.; Wright, A. Semiempirical modified embedded-atom potentials for silicon and germanium. *Phys. Rev. B* **1989**, *40*, 6085. [CrossRef]
25. Kim, Y.K.; Kim, H.K.; Jung, W.S.; Lee, B.J. Atomistic modeling of the Ti–Al binary system. *Comput. Mater. Sci.* **2016**, *119*, 1–8. [CrossRef]
26. Koizumi, Y.; Ogata, S.; Minamino, Y.; Tsuji, N. Energies of conservative and non-conservative antiphase boundaries in Ti3Al: A first principles study. *Philos. Mag.* **2006**, *86*, 1243–1259. [CrossRef]
27. Karkina, L.; Yakovenkova, L. Dislocation core structure and deformation behavior of Ti3Al. *Model. Simul. Mater. Sci. Eng.* **2012**, *20*, 065003. [CrossRef]
28. Legros, M.; Corn, A.; Caillard, D. Prismatic and basal slip in Ti3Al I. Frictional forces on dislocations. *Philos. Mag. A* **1996**, *73*, 61–80. [CrossRef]
29. Pei, Q.X.; Jhon, M.; Quek, S.S.; Wu, Z. A systematic study of interatomic potentials for mechanical behaviours of Ti-Al alloys. *Comput. Mater. Sci.* **2021**, *188*, 110239. [CrossRef]
30. Smith, J.S.; Isayev, O.; Roitberg, A.E. ANI-1: An extensible neural network potential with DFT accuracy at force field computational cost. *Chem. Sci.* **2017**, *8*, 3192–3203. [CrossRef] [PubMed]
31. Vita, J.A.; Trinkle, D.R. Spline-based neural network interatomic potentials: Blending classical and machine learning models. *Comput. Mater. Sci.* **2024**, *232*, 112655. [CrossRef]
32. Morawietz, T.; Artrith, N. Machine learning-accelerated quantum mechanics-based atomistic simulations for industrial applications. *J. -Comput.-Aided Mol. Des.* **2021**, *35*, 557–586. [CrossRef] [PubMed]
33. Zuo, Y.; Chen, C.; Li, X.; Deng, Z.; Chen, Y.; Behler, J.; Csányi, G.; Shapeev, A.V.; Thompson, A.P.; Wood, M.A.; et al. Performance and cost assessment of machine learning interatomic potentials. *J. Phys. Chem. A* **2020**, *124*, 731–745. [CrossRef]
34. Deringer, V.L.; Caro, M.A.; Csányi, G. Machine learning interatomic potentials as emerging tools for materials science. *Adv. Mater.* **2019**, *31*, 1902765. [CrossRef]
35. Behler, J. Perspective: Machine learning potentials for atomistic simulations. *J. Chem. Phys.* **2016**, *145*. [CrossRef]
36. Kobayashi, R.; Giofré, D.; Junge, T.; Ceriotti, M.; Curtin, W.A. Neural network potential for Al-Mg-Si alloys. *Phys. Rev. Mater.* **2017**, *1*, 053604. [CrossRef]
37. Dickel, D.; Nitol, M.; Barrett, C. LAMMPS implementation of rapid artificial neural network derived interatomic potentials. *Comput. Mater. Sci.* **2021**, *196*, 110481. [CrossRef]

38. Thompson, A.P.; Swiler, L.P.; Trott, C.R.; Foiles, S.M.; Tucker, G.J. Spectral neighbor analysis method for automated generation of quantum-accurate interatomic potentials. *J. Comput. Phys.* **2015**, *285*, 316–330. [CrossRef]
39. Bartók, A.P.; Payne, M.C.; Kondor, R.; Csányi, G. Gaussian approximation potentials: The accuracy of quantum mechanics, without the electrons. *Phys. Rev. Lett.* **2010**, *104*, 136403. [CrossRef] [PubMed]
40. Shapeev, A.V. Moment tensor potentials: A class of systematically improvable interatomic potentials. *Multiscale Model. Simul.* **2016**, *14*, 1153–1173. [CrossRef]
41. Qi, J.; Aitken, Z.; Pei, Q.; Tan, A.M.Z.; Zuo, Y.; Jhon, M.; Quek, S.; Wen, T.; Wu, Z.; Ong, S.P. Machine Learning Moment Tensor Potential for Modelling Dislocation and Fracture in $L1_0$-TiAl and $D0_{19}$-Ti_3Al Alloys. *arXiv* **2023**, arXiv:2305.11825.
42. Seko, A. Machine learning potentials for multicomponent systems: The Ti-Al binary system. *Phys. Rev. B* **2020**, *102*, 174104. [CrossRef]
43. Dickel, D.; Barrett, C.D.; Carino, R.L.; Baskes, M.I.; Horstemeyer, M.F. Mechanical instabilities in the modeling of phase transitions of titanium. *Model. Simul. Mater. Sci. Eng.* **2018**, *26*, 065002. [CrossRef]
44. Nitol, M.S.; Dickel, D.E.; Barrett, C.D. Machine learning models for predictive materials science from fundamental physics: An application to titanium and zirconium. *Acta Mater.* **2022**, *224*, 117347. [CrossRef]
45. Nitol, M.S.; Dang, K.; Fensin, S.J.; Baskes, M.I.; Dickel, D.E.; Barrett, C.D. Hybrid interatomic potential for Sn. *Phys. Rev. Mater.* **2023**, *7*, 043601. [CrossRef]
46. Nitol, M.S.; Mun, S.; Dickel, D.E.; Barrett, C.D. Unraveling Mg <c + a> slip using neural network potential. *Philos. Mag.* **2022**, *102*, 651–673. [CrossRef]
47. Nitol, M.S.; Dickel, D.E.; Barrett, C.D. Artificial neural network potential for pure zinc. *Comput. Mater. Sci.* **2021**, *188*, 110207. [CrossRef]
48. Hafner, J. Ab-initio simulations of materials using VASP: Density-functional theory and beyond. *J. Comput. Chem.* **2008**, *29*, 2044–2078. [CrossRef] [PubMed]
49. Perdew, J.P.; Burke, K.; Ernzerhof, M. Generalized gradient approximation made simple. *Phys. Rev. Lett.* **1996**, *77*, 3865. [CrossRef] [PubMed]
50. Dickel, D.; Francis, D.; Barrett, C. Neural network aided development of a semi-empirical interatomic potential for titanium. *Comput. Mater. Sci.* **2020**, *171*, 109157. [CrossRef]
51. Baskes, M.I. Determination of modified embedded atom method parameters for nickel. *Mater. Chem. Phys.* **1997**, *50*, 152–158. [CrossRef]
52. Lee, B.J.; Baskes, M.I. Second nearest-neighbor modified embedded-atom-method potential. *Phys. Rev. B* **2000**, *62*, 8564. [CrossRef]
53. Levenberg, K. A method for the solution of certain non-linear problems in least squares. *Q. Appl. Math.* **1944**, *2*, 164–168. [CrossRef]
54. Marquardt, D.W. An algorithm for least-squares estimation of nonlinear parameters. *J. Soc. Ind. Appl. Math.* **1963**, *11*, 431–441. [CrossRef]
55. Artrith, N.; Urban, A. An implementation of artificial neural-network potentials for atomistic materials simulations: Performance for TiO2. *Comput. Mater. Sci.* **2016**, *114*, 135–150. [CrossRef]
56. Becker, C.A.; Tavazza, F.; Trautt, Z.T.; Buarque de Macedo, R.A. Considerations for choosing and using force fields and interatomic potentials in materials science and engineering. *Curr. Opin. Solid State Mater. Sci.* **2013**, *17*, 277–283. [CrossRef]
57. Hale, L.M.; Trautt, Z.T.; Becker, C.A. Evaluating variability with atomistic simulations: The effect of potential and calculation methodology on the modeling of lattice and elastic constants. *Model. Simul. Mater. Sci. Eng.* **2018**, *26*, 055003. [CrossRef]
58. Sadigh, B.; Erhart, P.; Stukowski, A.; Caro, A.; Martinez, E.; Zepeda-Ruiz, L. Scalable parallel Monte Carlo algorithm for atomistic simulations of precipitation in alloys. *Phys. Rev. B* **2012**, *85*, 184203. [CrossRef]
59. Metropolis, N.; Rosenbluth, A.W.; Rosenbluth, M.N.; Teller, A.H.; Teller, E. Equation of state calculations by fast computing machines. *J. Chem. Phys.* **1953**, *21*, 1087–1092. [CrossRef]
60. Kiely, E.; Zwane, R.; Fox, R.; Reilly, A.M.; Guerin, S. Density functional theory predictions of the mechanical properties of crystalline materials. *CrystEngComm* **2021**, *23*, 5697–5710. [CrossRef]
61. Jafari, M.; Zarifi, N.; Nobakhti, M.; Jahandoost, A.; Lame, M. Pseudopotential calculation of the bulk modulus and phonon dispersion of the bcc and hcp structures of titanium. *Phys. Scr.* **2011**, *83*, 065603. [CrossRef]
62. Simmons, G.; Wang, H. *Single Crystal Elastic Constants and Calculated Aggregate Properties: A Handbook*; MIT Press: Cambridge, MA, USA, 1971.
63. Yin, B.; Wu, Z.; Curtin, W. Comprehensive first-principles study of stable stacking faults in hcp metals. *Acta Mater.* **2017**, *123*, 223–234. [CrossRef]
64. Kittel, C. *Introduction to Solid State Physics*; John Wiley & Sons, Inc: Hoboken, NJ, USA, 2005.
65. Fisher, E.; Renken, C. Single-crystal elastic moduli and the hcp → bcc transformation in Ti, Zr, and Hf. *Phys. Rev.* **1964**, *135*, A482. [CrossRef]

66. Boer, F.R. *Cohesion in Metals: Transition Metal Alloys*; North Holland: Amsterdam, The Netherlands, 1988; Volume 1.
67. Tyson, W.; Miller, W. Surface free energies of solid metals: Estimation from liquid surface tension measurements. *Surf. Sci.* **1977**, *62*, 267–276. [CrossRef]
68. Blakemore, J.S. *Solid State Physics*; Cambridge University Press: Cambridge, UK, 1985.
69. Malica, C.; Dal Corso, A. Quasi-harmonic temperature dependent elastic constants: Applications to silicon, aluminum, and silver. *J. Phys. Condens. Matter* **2020**, *32*, 315902. [CrossRef]
70. Li, W.; Wang, T. Ab initio investigation of the elasticity and stability of aluminium. *J. Phys. Condens. Matter* **1998**, *10*, 9889. [CrossRef]
71. Wang, H.; Li, M. Ab initio calculations of second-, third-, and fourth-order elastic constants for single crystals. *Phys. Rev. B* **2009**, *79*, 224102. [CrossRef]
72. Golesorkhtabar, R.; Pavone, P.; Spitaler, J.; Puschnig, P.; Draxl, C. ElaStic: A tool for calculating second-order elastic constants from first principles. *Comput. Phys. Commun.* **2013**, *184*, 1861–1873. [CrossRef]
73. Shang, S.; Saengdeejing, A.; Mei, Z.; Kim, D.; Zhang, H.; Ganeshan, S.; Wang, Y.; Liu, Z. First-principles calculations of pure elements: Equations of state and elastic stiffness constants. *Comput. Mater. Sci.* **2010**, *48*, 813–826. [CrossRef]
74. Lu, G.; Kioussis, N.; Bulatov, V.V.; Kaxiras, E. Generalized-stacking-fault energy surface and dislocation properties of aluminum. *Phys. Rev. B* **2000**, *62*, 3099. [CrossRef]
75. Wu, X.Z.; Wang, R.; Wang, S.F.; Wei, Q.Y. Ab initio calculations of generalized-stacking-fault energy surfaces and surface energies for FCC metals. *Appl. Surf. Sci.* **2010**, *256*, 6345–6349. [CrossRef]
76. Smallman, R.; Dobson, P. Stacking fault energy measurement from diffusion. *Metall. Trans.* **1970**, *1*, 2383–2389. [CrossRef]
77. Woodward, C.; Trinkle, D.; Hector, L., Jr.; Olmsted, D. Prediction of dislocation cores in aluminum from density functional theory. *Phys. Rev. Lett.* **2008**, *100*, 045507. [CrossRef] [PubMed]
78. Crampin, S.; Hampel, K.; Vvedensky, D.; MacLaren, J. The calculation of stacking fault energies in close-packed metals. *J. Mater. Res.* **1990**, *5*, 2107–2119. [CrossRef]
79. Denteneer, P.; Soler, J. Defect energetics in aluminium. *J. Phys. Condens. Matter* **1991**, *3*, 8777. [CrossRef]
80. Hammer, B.; Jacobsen, K.; Milman, V.; Payne, M. Stacking fault energies in aluminium. *J. Phys. Condens. Matter* **1992**, *4*, 10453. [CrossRef]
81. Hehenkamp, T. Absolute vacancy concentrations in noble metals and some of their alloys. *J. Phys. Chem. Solids* **1994**, *55*, 907–915. [CrossRef]
82. Tanaka, K.; Okamoto, K.; Inui, H.; Minonishi, Y.; Yamaguchi, M.; Koiwa, M. Elastic constants and their temperature dependence for the intermetallic compound Ti_3Al. *Philos. Mag. A* **1996**, *73*, 1475–1488. [CrossRef]
83. Wei, Y.; Zhang, Y.; Lu, G.H.; Xu, H. SITE PREFERENCE AND ELASTIC PROPERTIES OF A 2-Ti 3 Al WITH OXYGEN IMPURITY: A FIRST-PRINCIPLES STUDY. *Int. J. Mod. Phys. B* **2010**, *24*, 2749–2755. [CrossRef]
84. Zhang, C.; Hou, H.; Zhao, Y.; Yang, X.; Guo, Y. First-principles study on structural, elastic and thermal properties of γ-TiAl and α_2-Ti_3Al phases in TiAl-based alloy under high pressure. *Int. J. Mod. Phys. B* **2017**, *31*, 1750079. [CrossRef]
85. Pearson, W.B. *A Handbook of Lattice Spacings and Structures of Metals and Alloys: INTERNATIONAL Series of Monographs on Metal Physics and Physical Metallurgy*; Elsevier: Amsterdam, The Netherlands, 2013; Volume 4.
86. Tanaka, K. Single-crystal elastic constants of γ-TiAl. *Philos. Mag. Lett.* **1996**, *73*, 71–78. [CrossRef]
87. Fu, H.; Zhao, Z.; Liu, W.; Peng, F.; Gao, T.; Cheng, X. Ab initio calculations of elastic constants and thermodynamic properties of γTiAl under high pressures. *Intermetallics* **2010**, *18*, 761–766. [CrossRef]
88. Li, J.; Zhang, M.; Luo, X. Theoretical investigations on phase stability, elastic constants and electronic structures of D022-and L12-Al3Ti under high pressure. *J. Alloys Compd.* **2013**, *556*, 214–220. [CrossRef]
89. Tang, P.Y.; Tang, B.Y.; Su, X.P. First-principles studies of typical long-period superstructures Al5Ti3, h-Al2Ti and r-Al2Ti in Al-rich TiAl alloys. *Comput. Mater. Sci.* **2011**, *50*, 1467–1476. [CrossRef]
90. Kwasniak, P.; Garbacz, H.; Kurzydlowski, K. Solid solution strengthening of hexagonal titanium alloys: Restoring forces and stacking faults calculated from first principles. *Acta Mater.* **2016**, *102*, 304–314. [CrossRef]
91. Rao, S.; Venkateswaran, A.; Letherwood, M. Molecular statics and molecular dynamics simulations of the critical stress for motion of a/3$\langle$1 1 2 0$\rangle$ screw dislocations in α-Ti at low temperatures using a modified embedded atom method potential. *Acta Mater.* **2013**, *61*, 1904–1912. [CrossRef]
92. Spreadborough, J.; Christian, J. The measurement of the lattice expansions and Debye temperatures of titanium and silver by X-ray methods. *Proc. Phys. Soc.* **1959**, *74*, 609. [CrossRef]
93. Kornilov, I.; Pylaeva, E.; Volkova, M. Phase diagram of the binary system titanium-aluminum. *Bull. Acad. Sci. Ussr, Div. Chem. Sci.* **1956**, *5*, 787–795. [CrossRef]
94. Rostoker, W. Observations on the lattice parameters of the alpha solid solution in the titanium-aluminum system. *Jom* **1952**, *4*, 212–213. [CrossRef]

95. Hennig, R.; Lenosky, T.; Trinkle, D.; Rudin, S.; Wilkins, J. Classical potential describes martensitic phase transformations between the α, β, and ω titanium phases. *Phys. Rev. B* **2008**, *78*, 054121. [CrossRef]
96. Stukowski, A. Visualization and analysis of atomistic simulation data with OVITO-the Open Visualization Tool. *Model. Simul. Mater. Sci. Eng.* **2010**, *18*, 015012. [CrossRef]
97. Kainuma, R.; Palm, M.; Inden, G. Solid-phase equilibria in the Ti-rich part of the Ti Al system. *Intermetallics* **1994**, *2*, 321–332. [CrossRef]
98. Blackburn, M. The ordering transformation in titanium- aluminum alloys containing up to 25 at. pct aluminum(Ti-Al alloys ordering transformation studied by electron microscopy and electron and X-ray diffraction, showing existence of three phase fields). *Aime Trans.* **1967**, *239*, 1200–1208.
99. Shull, R.; McAlister, A.; Reno, R. Phase equilibria in the titanium-aluminum system. In *Titanium: Science and Technology*; Deutsche Gesellschaft für Metallkunde: Sankt Augustin, Germany, 1985; pp. 1459–1466.
100. Ohnuma, I.; Fujita, Y.; Mitsui, H.; Ishikawa, K.; Kainuma, R.; Ishida, K. Phase equilibria in the Ti–Al binary system. *Acta Mater.* **2000**, *48*, 3113–3123. [CrossRef]

Disclaimer/Publisher's Note: The statements, opinions and data contained in all publications are solely those of the individual author(s) and contributor(s) and not of MDPI and/or the editor(s). MDPI and/or the editor(s) disclaim responsibility for any injury to people or property resulting from any ideas, methods, instructions or products referred to in the content.